Chemical Science

ROYAL SOCIETY OF CHEMISTRY

EDGE ARTICLE

View Article Online
View Journal | View Issue

Cite this: *Chem. Sci.*, 2023, **14**, 4308

All publication charges for this article have been paid for by the Royal Society of Chemistry

Ligand engineering of Au_{44} nanoclusters for NIR-II luminescent and photoacoustic imaging-guided cancer photothermal therapy†

Ge Yang,[a] Xueluer Mu,[b] Xinxin Pan,[a] Ying Tang,[b] Qiaofeng Yao,[c] Yaru Wang,[a] Fuyi Jiang,[d] Fanglin Du,[a] Jianping Xie, *[ce] Xianfeng Zhou *[b] and Xun Yuan *[a]

Received 15th October 2022
Accepted 14th February 2023

DOI: 10.1039/d2sc05729h

rsc.li/chemical-science

Developing a high-performance noninvasive probe for precise cancer theranostics is very challenging but urgently required. Herein, a novel Au nanoclusters (NCs)-based probe was designed for cancer theranostics *via* ligand engineering by conjugating photoluminescent (PL) Au_{44} NCs in the second near-infrared window (NIR-II, 1000–1700 nm) with aromatic photoacoustic (PA)/photothermal molecules through click chemistry. This design bypasses the incompatibility dilemma between photoluminescence (PL) attributes and PA/photothermal properties because the rigidity of the PA/photothermal molecules can lead to aggregation-induced emission (AIE) of the Au(I)-ligand shell of the Au NCs by constraining their nonradiative relaxation. Benefiting from strong NIR-II PL with emissions at 1080 and 1240 nm, high photothermal conversion efficiency (65.12%), low cytotoxicity, appropriate renal clearance, and enhanced permeability and retention (EPR) effect, the as-designed Au NC-based theranostic probe achieves ultradeep NIR-II PL/PA imaging-guided cancer photothermal therapy (PTT). Remarkably, 16 days after photothermal treatment guided by NIR-II PL/PA imaging, mice were all healed without tumor recurrence, while the average life span of the mice in the control groups was only 17–21 days. This study is interesting because it provides a paradigm for designing a metal NC-based theranostics probe, and it may add fundamentally and methodologically to noninvasive imaging-guided disease therapy.

Introduction

Noninvasive yet precise theranostics for cancer (NPTC) is desired for both cancer patients and therapists because of its avoidance of physical trauma, low cost, and real-time feedback-mediated higher therapeutic efficacy.[1] However, developing a high-performance NPTC probe is a great challenge due to the following aspects: (1) neither noninvasive disease diagnosis with deep tissue penetration and high spatiotemporal resolution nor tumor therapy with high tumor selectivity and few side effects are easy tasks;[2] (2) simply integrating the diagnostic entity and a therapeutic counterpart into one probe usually results in incompatibility of the constructed NPTC probe, such as the mutual energy competition between the photoluminescence (PL) imaging and the photothermal therapy (PTT) based on the Jablonski energy spectrum theory;[3] (3) the theranostic probe should also be renal clearable (*i.e.*, a hydrodynamic size of ≤5.5 nm is the kidney filtration threshold) with benign biocompatibility.[4] Overall, tackling any one of such issues presents a challenge, let alone simultaneously solving all these issues in designing NPTC probes, which further reflects the difficulties and significance in the construction of high-performance NPTC probes.

Recently, ultrasmall Au nanoclusters (NCs) with a core size of ≤3 nm have emerged as a novel class of functional nanomaterials in the biomedical field due to their atomic-precision size,[5] rich yet tailorable surface chemistry,[6] and unique molecule-like properties, such as strong PL signal,[7] chirality,[8] and highest occupied molecular orbital-lowest unoccupied molecular orbital (HOMO–LUMO) transitions.[9] Such intriguing physicochemical properties allow Au NCs to be biocompatible,[10] surface engineerable,[6b,11] and renal clearable (*i.e.*, hydrodynamic size of ≤5.5 nm),[4a,12] making their

[a]*School of Materials Science and Engineering, Qingdao University of Science and Technology, Qingdao, 266042, PR China. E-mail: yuanxun@qust.edu.cn*

[b]*Key Lab of Biobased Polymer Materials of Shandong Provincial Education Department, School of Polymer Science and Engineering, Qingdao University of Science and Technology, Qingdao, 266042, PR China. E-mail: xianfeng@qust.edu.cn*

[c]*Joint School of National University of Singapore and Tianjin University, International Campus of Tianjin University, Binhai New City, Fuzhou, 350207, PR China. E-mail: chexiej@nus.edu.sg*

[d]*School of Environment and Material Engineering, Yantai University, Yantai, 264005, PR China*

[e]*Department of Chemical and Biomolecular Engineering, National University of Singapore, 4 Engineering Drive 4, Singapore, 117585, Singapore*

† Electronic supplementary information (ESI) available: The native PAGE and ESI mass of $Au_{44}MBA_{26}$ NCs; synthetic route and characteristics of the alkynylated Cy7 molecules; FTIR spectra and UV-vis absorption spectra of Au_{44} NCs; NIR-II PL emission spectra of $Au_{44}MBA_{26}$-Cy7 NCs in mixed solvents; PTT of $Au_{44}MBA_{26}$ NCs *in vitro*; PA images of $Au_{44}MBA_{26}$ NCs; supplementary notes. See DOI: https://doi.org/10.1039/d2sc05729h

application possible for disease diagnosis or therapy.[13] For example, several recently developed types of Au NCs with PL emission in the second near-infrared window (NIR-II, 1000–1700 nm) have shown overwhelming advantages in bioimaging in terms of deep tissue penetration (>1 cm) and high spatio-temporal resolution (approximately 10 μm, and 4 ms) compared with NIR-I emitting NC-based probes (650–900 nm), which have a limited *in vivo* signal-to-noise ratio.[14] We thus hypothesize that if we can design atomically precise NIR-II emitting Au NCs as a molecular matrix for delicate engineering, we may develop a high-performance NPTC probe to achieve NIR-II PL imaging-guided tumor therapy. For proof-of-concept purposes, here a noninvasive PTT modality was chosen as the therapy function of the NPTC probe because it is advantageous in cancer treatment with high tumor selectivity and few side effects.[2c,15] More importantly, the photothermal attributes may endow the NPTC probes with an additional PA signal for improving diagnostic efficacy due to the thermoelastic expansion-induced PA emission of the treated tissues.[2a,16] In addition, the NIR-II PL properties of the NPTC probes may in turn remedy the limitations of the poor light absorption of conventional PTT probes in deep tissues, expectedly achieving dual-mode NIR-II PL/PA imaging-guided cancer PTT. However, it is still a major challenge to design NIR-II emitting Au NCs with atomic precision. Moreover, several other issues may also arise, *e.g.*, how to engineer NIR-II emitting Au NCs to concurrently achieve NIR-II PL/PA imaging with excellent PTT, can the NIR-II PL imaging proceed synchronously with PA imaging, how the NIR-II PL imaging affects the PTT *in vivo*, and what are the theranostic efficacy and pharmacokinetic behavior of the Au NC-based probe for NPTC like after engineering.

In this work, we report the design of a novel Au NC-based theranostic probe – $Au_{44}MBA_{26}$-Cy7 (here MBA denotes 4-mercaptobenzoic acid; Cy7 denotes heptamethine dye) for ultradeep NIR-II PL and PA imaging-guided cancer PTT. The $Au_{44}MBA_{26}$-Cy7 probe comprises NIR-II emitting $Au_{44}MBA_{26}$ NCs linked with aromatic Cy7 molecules through click chemistry (Scheme 1), which not only enhances the NIR-II PL signal of the Au_{44} NCs by closing the nonradiative pathway of the inner Au NCs based on AIE,[17] but also improves the photothermal conversion efficiency of the outer Cy7 shell. Such intriguing NIR-II PL/photothermal attributes, together with benign biocompatibility, good pharmacokinetics, efficient renal clearance, and enhanced permeability and retention (EPR) effect, make this probe capable of NIR-II PL and PA imaging-guided cancer therapy with high sensitivity and specificity without damaging major organs. To the best of our knowledge, this may be the first successful Au NC probe for NPTC involving simultaneous NIR-II PL/PA imaging-based diagnosis and PTT-based therapy, which would become a promising next-generation noninvasive theranostics technique for cancer.

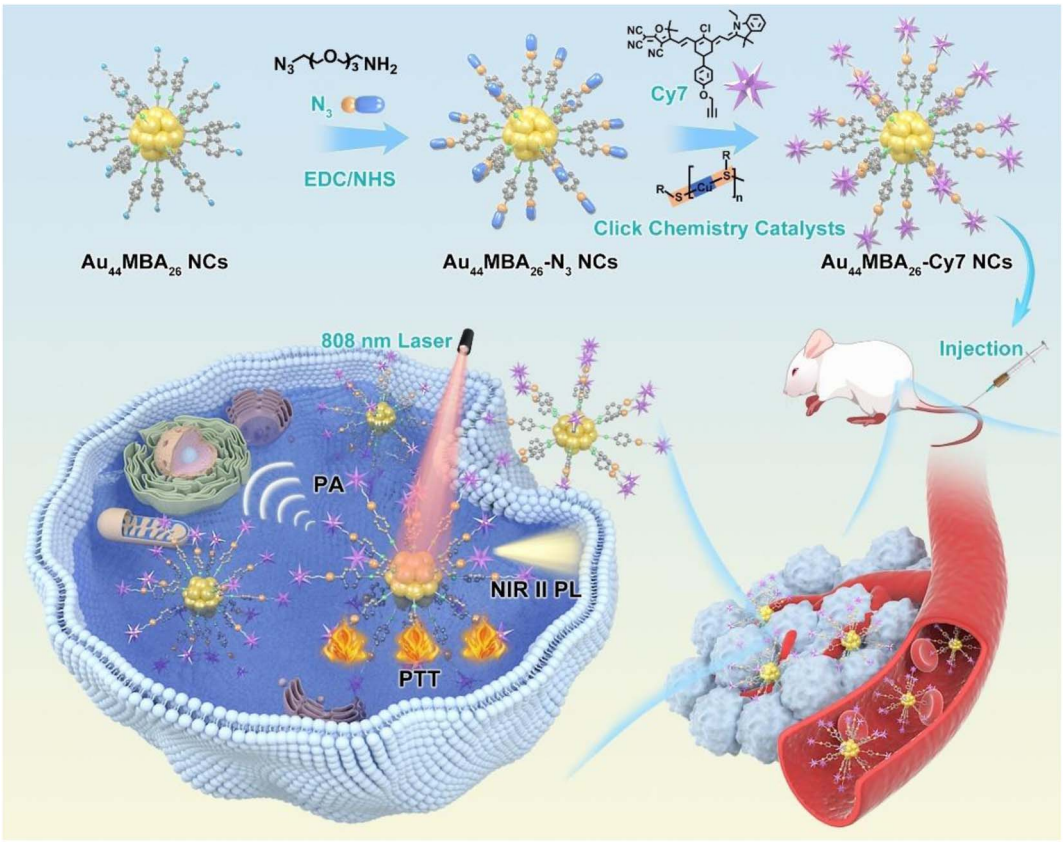

Scheme 1 Schematic illustration of the synthesis of $Au_{44}MBA_{26}$-Cy7 NCs based on the click chemistry-mediated conjugation of $Au_{44}MBA_{26}$ NCs with Cy7 molecules, and the application of NIR-II PL and PA imaging-guided cancer PTT.

Results and discussion

The synthesis of NIR-II emitting metal NCs with atomic precision is a long-standing challenge in the cluster community due to the poor understanding of the correlation between their precise size/structure and PL mechanism. In this study, NIR-II emitting $Au_{44}MBA_{26}$ NCs were synthesized *via* an NaOH-mediated $NaBH_4$ reduction method.[6b,18] As shown in Fig. 1a, three step-like optical peaks at 497 nm, 590 nm and 794 nm are observed in the UV-vis absorption spectrum of the Au NCs, indicating the successful synthesis of monodisperse Au NCs.[19] While the single band in the native polyacrylamide gel electrophoresis (PAGE) results clearly reveals the high monodispersity of the Au NCs (Fig. S1 in the ESI†), the electrospray ionization mass spectrometry (ESI-MS) results disclose the synthesis of high-quality $Au_{44}MBA_{26}$ NCs, in which two peaks at m/z = ~3162 and ~4216 can be ambiguously assigned as $[Au_{44}MBA_{26}–2H]^{4-}$ and $[Au_{44}MBA_{26}–H]^{3-}$ species, respectively (Fig. 1b). In addition, the hydrodynamic diameter of the Au_{44} NCs was confirmed to be 2.73 nm (Fig. 1c), while their core sizes were all below 2 nm with an average size of 1.58 nm (Fig. 1d). More interestingly, the Au_{44} NCs display two PL emission peaks at 1080 nm and 1280 nm when excited at 808 nm (Fig. 1f), manifesting that the Au_{44} NCs are a promising PL probe for NIR-II PL imaging. Taking all the characterization results together, the Au_{44} NCs exhibit molecular optical absorption, atom-precision formula, good hydrophilicity, ultrasmall hydrodynamic size (<3 nm), and strong NIR-II PL intensity, making them an ideal probe for biomedical applications.

Upon acquiring $Au_{44}MBA_{26}$ NCs, we introduced azide groups on the surface of the Au_{44} NCs *via* a simple 1-(3-dimethylaminopropyl)-3-ethylcarbodiimide hydrochloride (EDC)/*N*-hydroxysuccinimide (NHS) crosslinking strategy, and then conjugated the Au_{44} NCs with aromatic PA/photothermal alkynylated Cy7 molecules *via* click chemistry to obtain multifunctional $Au_{44}MBA_{26}$-Cy7 (Scheme 1, Fig. S2–S6 and

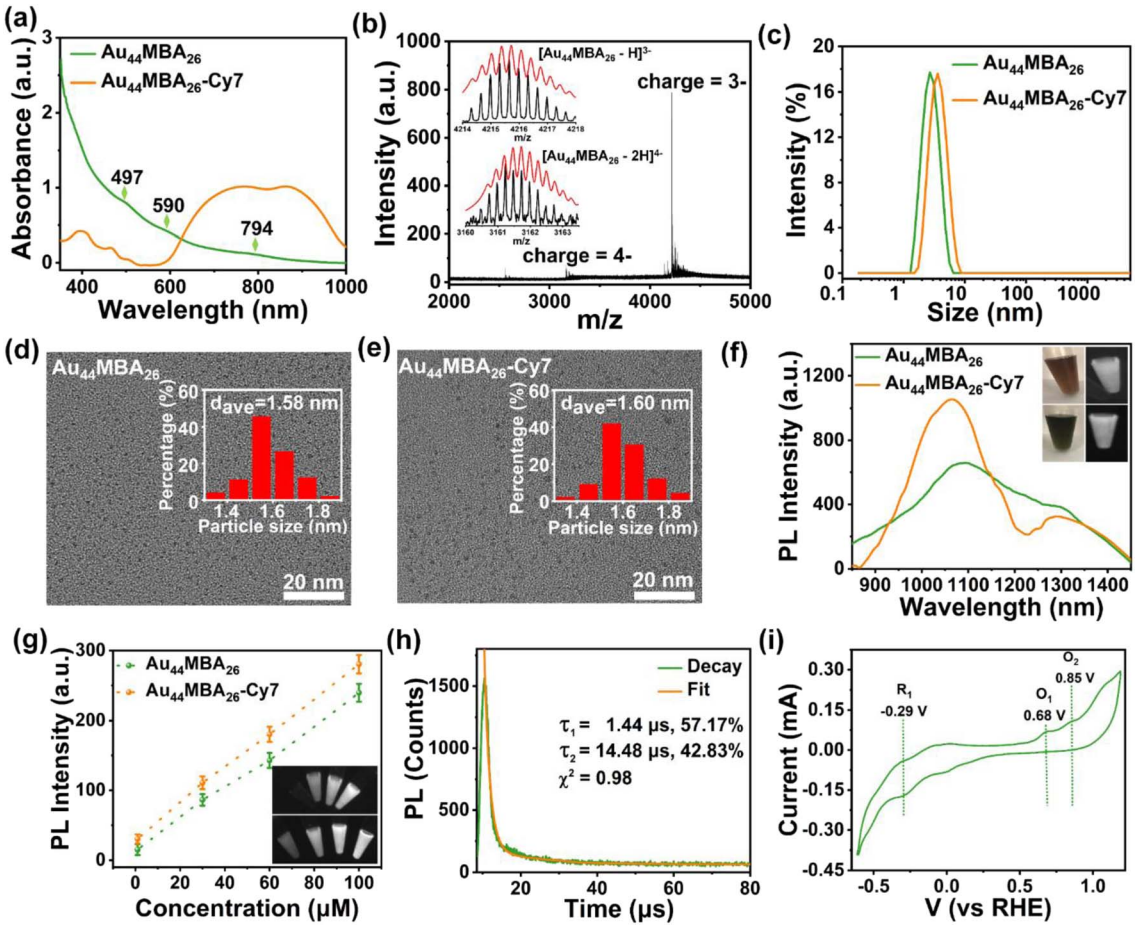

Fig. 1 (a) UV-vis absorption spectra of pristine $Au_{44}MBA_{26}$ NCs and $Au_{44}MBA_{26}$-Cy7 NCs. (b) ESI-MS of $Au_{44}MBA_{26}$ NCs. The inset shows experimentally acquired (black curve) and simulated (red curve) isotope patterns of the NCs. (c) Dynamic light scattering (DLS) profiles, (d) and (e) TEM images with inserted size distribution histograms, and (f) NIR-II photoemission spectra ($\lambda_{excitation}$ = 808 nm) of pristine $Au_{44}MBA_{26}$ NCs and $Au_{44}MBA_{26}$-Cy7 NCs. The inset in (f) shows the photographs of pristine $Au_{44}MBA_{26}$ (upper panel) and $Au_{44}MBA_{26}$-Cy7 solutions (lower panel) under visible (left) and NIR light (right) illumination. (g) NIR-II imaging contrast and corresponding NIR-II images (inset; taken under 808 nm laser illumination; upper panel: $Au_{44}MBA_{26}$; lower panel: $Au_{44}MBA_{26}$-Cy7) of pristine $Au_{44}MBA_{26}$ NCs and $Au_{44}MBA_{26}$-Cy7 NCs at concentrations of 0, 30, 60 and 100 μM. (h) NIR-II PL decay profile and the corresponding fit of pristine $Au_{44}MBA_{26}$ NCs. (i) Cyclic voltammogram of pristine $Au_{44}MBA_{26}$ NCs (reference potentials, HER: potential of hydrogen evolution reaction at pH = 0).

Supplementary Note I in the ESI†). After conjugation, the as obtained $Au_{44}MBA_{26}$-Cy7 sample displays broad yet intensive optical absorption in the range of 600–1000 nm in its UV-vis absorption spectrum (Fig. 1a), which is dramatically different from that of pristine $Au_{44}MBA_{26}$ NCs and was attributed to the contribution of the Cy7 molecules (Fig. S7a†). Furthermore, while the Cy7 modification did not change the core size of the $Au_{44}MBA_{26}$ NCs (Fig. 1d and e), a slight increase in the hydrodynamic diameter from 2.73 nm to 3.45 nm of the modified $Au_{44}MBA_{26}$ NCs was observed (Fig. 1c), which ensures the good renal clearance of $Au_{44}MBA_{26}$-Cy7 NCs because their hydrodynamic diameter is still below the kidney filtration threshold (~5.5 nm).[4a] In addition, it was confirmed that around 13 Cy7 molecules were conjugated on each $Au_{44}MBA_{26}$ NC (Fig. S8 and Supplementary Note II in the ESI†), indicating the good structural symmetry of $Au_{44}MBA_{26}$-Cy7.

The NIR-II PL emission peaks of the $Au_{44}MBA_{26}$ NCs at 1080 nm and 1280 nm were retained after Cy7 modification, accompanied by partial enhancement in the emission intensity (Fig. 1f). Indeed, surface engineering has been proven to be an efficient strategy by which to enhance the PL of metal NCs. For example, Pyo *et al.* reported that the PL of $Au_{22}GSH_{18}$ NCs (here GSH denotes glutathione) was enhanced by more than five times in water upon surface engineering *via* conjugating benzyl chloroformate (CBz-Cl) and pyrene (Py), attributed to the ligand shell rigidification effect as well as the promoted energy transfer from the ligands to the metal core.[20] Inspired by this, we speculated that the enhanced NIR-II PL of $Au_{44}MBA_{26}$-Cy7 could be due to the stronger absorption in the range of 600–1000 nm, the promoted charge transfer of the Cy7 molecules, and the resulting aggregation-induced emission (AIE) effect. Specifically, upon conjugating the $Au_{44}MBA_{26}$ NCs with rigid Cy7 molecules, the high π-electronic delocalization of the 2-(3-cyano-4,5,5-trimethylfuran-2(5*H*)-ylidene) malononitrile (TCF) group in the Cy7 molecules enhanced the charge transfer from the ligands to the metal core of the NCs.[15a] Moreover, the as-obtained $Au_{44}MBA_{26}$-Cy7 NCs showed remarkable AIE effect (Fig. S9†), *i.e.*, the $Au_{44}MBA_{26}$-Cy7 NCs displayed weak PL emission in *N*,*N*-dimethylformamide (DMF) with good solubility, but a more intense PL signal in mixed DMF/H_2O with relatively poor solubility, which is due to the rigidity of the Cy7 shell endowing the $Au_{44}MBA_{26}$-Cy7 NCs with AIE properties by closing the nonradiative pathways of the inner NCs.[21] It should be emphasized that the acquisition of AIE properties by conjugating the $Au_{44}MBA_{26}$ NCs with rigid Cy7 molecules is the key to the design, which not only enhances the NIR-II PL intensity *via* AIE, but also ensures the maintenance of excellent PA/photothermal signals of the outer Cy7 shell (discussed later), bypassing the dilemma of the incompatibility between the PA/photothermal properties and PL attributes. Meanwhile, as shown in Fig. 1g, both $Au_{44}MBA_{26}$ and $Au_{44}MBA_{26}$-Cy7 show concentration-dependent NIR-II PL imaging contrast, allowing their usage in NIR-II PL imaging at an extremely low concentration (*e.g.*, 30 μM).

Considering that the NIR-II PL signal of the $Au_{44}MBA_{26}$-Cy7 NCs originates from the $Au_{44}MBA_{26}$ NCs instead of the Cy7 molecules that exhibit emission at 931 nm (Fig. S7b†), we may uncover the NIR-II PL mechanism of the $Au_{44}MBA_{26}$-Cy7 NCs by investigating $Au_{44}MBA_{26}$. On this basis, both the NIR-II PL lifetime and the highest unoccupied molecular orbital-lowest unoccupied molecular orbital (HOMO–LUMO) transition of the $Au_{44}MBA_{26}$ NCs were analyzed. As shown in Fig. 1h, the NIR-II PL decay profile of the $Au_{44}MBA_{26}$ NCs reveals that the NCs are composed of microsecond lifetime components (1.44 μs: 57.17%; 14.48 μs: 42.83%). The long PL lifetime and a large Stokes shift (>200 nm) indicate that the NIR-II PL emission of the $Au_{44}MBA_{26}$ NCs most probably results from ligand-to-metal charge transfer or ligand-to-metal-metal charge transfer and subsequent radiative relaxation. In addition, we conducted cyclic voltammetry (CV) tests to assess the HOMO–LUMO gaps of the $Au_{44}MBA_{26}$ NCs that may correlate to their PL properties[22] (Fig. 1i). The results show a reduction potential of 0.29 V and two oxidation potentials at 0.68 V and 0.85 V (*vs.* the reversible hydrogen electrode, RHE). Of note, such reduction and oxidation peaks have been used to determine the positions of the LUMO and HOMO.[22] On this basis, two energy transition gaps of the $Au_{44}MBA_{26}$ NCs were identified to be 0.97 eV (*i.e.*, the first transition) and 1.14 eV (*i.e.*, the second transition), which are consistent with the NIR-II PL emissions at 1080 nm and 1280 nm shown in Fig. 1f. However, it is still difficult to establish the precise correlation between the NIR-II PL properties and the structure of the $Au_{44}MBA_{26}$ NCs, although the $Au_{44}MBA_{26}$ NCs may share the same crystal structure as the reported Au_{44}(2,4-dimethylbenzenethiol)$_{26}$ NCs.[23] Such correlation may be established with additional efforts on theoretical simulations.

The $Au_{44}MBA_{26}$-Cy7 NCs exhibit excellent photothermal properties. As shown in Fig. 2a, the temperature of the aqueous $Au_{44}MBA_{26}$-Cy7 solution (10 μM) elevates dramatically from 30 °C to 70 °C within 10 min of 808 nm laser irradiation, outperforming the photothermal efficacy of pristine $Au_{44}MBA_{26}$ NCs, which only cause a temperature increase of up to 43 °C under the same conditions (Fig. S10†). It should be emphasized that such an excellent photothermal trait of the $Au_{44}MBA_{26}$-Cy7 NCs guarantees their high-efficiency killing of tumor cells, and could overcome the challenges caused by the high expression of heat shock proteins (HSPs).[24] HSPs are a class of heat-stress proteins that are widespread, from bacteria to mammals, and could modulate the tumor cell response to heat-induced cytotoxicity.[24] In addition, the temperature response of the $Au_{44}MBA_{26}$-Cy7 NCs under NIR laser irradiation exhibits good correlation with their concentration (Fig. 2a) and laser power (Fig. 2b). In order to study the photothermal stability of the $Au_{44}MBA_{26}$-Cy7 NCs, we carried out repeated radiation-cooling experiments. As shown in Fig. 2c, while both the $Au_{44}MBA_{26}$-Cy7 NCs and pristine $Au_{44}MBA_{26}$ NCs show good photothermal stability in these five radiation-cooling cycles, the photothermal activity of the $Au_{44}MBA_{26}$-Cy7 NCs is much higher than that of pristine $Au_{44}MBA_{26}$ NCs with the same concentration. In terms of the photothermal conversion efficiency,[15a,25] the $Au_{44}MBA_{26}$-Cy7 NCs (65.12%) also perform better than pristine $Au_{44}MBA_{26}$ NCs (34.96%) based on the heat transfer time constant and maximum steady-state temperature results (Fig. 2d), which reveal the major role of Cy7 conjugation in enhancing the

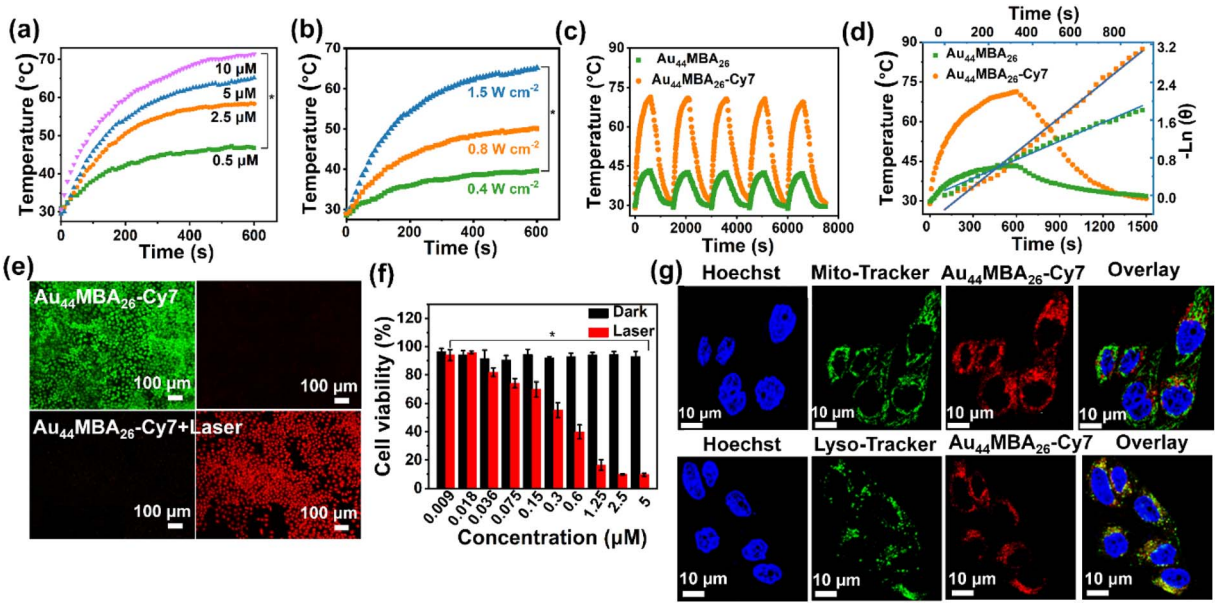

Fig. 2 *In vitro* PTT of the $Au_{44}MBA_{26}$-Cy7 NCs. Photothermal heating profiles of the $Au_{44}MBA_{26}$-Cy7 NCs in water at (a) different concentrations under laser irradiation (808 nm, 1.5 W cm^{-2}) and (b) different power density irradiations (here the NC concentration was fixed to 5 μM). Error bars, mean ± SD ($n = 3$), *$P < 0.05$. (c) The cycled heating/cooling curves of pristine $Au_{44}MBA_{26}$ and $Au_{44}MBA_{26}$-Cy7 NCs in water. (d) Photothermal efficiency evaluation of the $Au_{44}MBA_{26}$ and $Au_{44}MBA_{26}$-Cy7 NCs in water after irradiation for 10 min and being cooled to room temperature. The photothermal efficiency was obtained from the linear fitting of the cooling time *versus* the negative natural logarithm of the temperature. (e) PL microscope images of viable HeLa cells stained with Calcein AM (green color) and nonviable HeLa cells stained with EthD-1 (red) treated with 5 μM $Au_{44}MBA_{26}$-Cy7 NCs in the dark (upper panel) or under laser irradiation (lower panel) for 6 min (808 nm, 1.5 W cm^{-2}). (f) *In vitro* cytotoxicity and photothermal assays of $Au_{44}MBA_{26}$-Cy7 NCs with different concentrations (0.009–5 μM) on HeLa cells evaluated by MTT Kit NCs in the dark or under laser irradiation. Error bars indicate the mean ± SD ($n = 8$), *$P < 0.05$. (g) Confocal PL images of $Au_{44}MBA_{26}$-Cy7 NCs (0.5 μM) in live HeLa cells co-stained with MitoTracker Green or LysoTracker Green.

photothermal conversion efficiency of the $Au_{44}MBA_{26}$-Cy7 NCs. Of note, the conjugation of rigid Cy7 with the $Au_{44}MBA_{26}$ NCs not only endows the $Au_{44}MBA_{26}$-Cy7 NCs with AIE properties to avoid the possible energy competition between the PL attributes and PA/photothermal signals, but also creates a highly localized concentration of Cy7 molecules that is more favorable for high photothermal efficiency than that of unconjugated analogues, providing a paradigm in the design of a multifunctional probe for NPTC.

Naturally, we assessed the *in vitro* PTT effect as well as cytotoxicity of the $Au_{44}MBA_{26}$-Cy7 NCs by conducting both live/dead staining and 3-[4,5-dimethylthiazole-2-yl]-2,5-diphenyl tetrazolium bromide (MTT) assays using HeLa cells as a model. As shown in Fig. 2e, the live/dead staining results show that the HeLa cells treated with the $Au_{44}MBA_{26}$-Cy7 NCs but without exposure to laser irradiation are almost all alive (green color), which suggests that the $Au_{44}MBA_{26}$-Cy7 NCs exhibit very low cytotoxicity. By contrast, upon laser irradiation for 6 min, the HeLa cells treated with the $Au_{44}MBA_{26}$-Cy7 NCs were all dead (red color, Fig. 2e), which is very different from those treated with the pristine $Au_{44}MBA_{26}$ NCs, where only a small number of dead HeLa cells stained in red were observed (Fig. S11a†). These results indicate that the $Au_{44}MBA_{26}$-Cy7 NCs have excellent *in vitro* PTT effect. In addition, MTT assay provides quantitative data on the PTT effect. As shown in Fig. 2f, the $Au_{44}MBA_{26}$-Cy7 NCs display neglectable cytotoxicity, which is evidenced by the fact that no apparent reduction in the HeLa cell viability is observed even upon increasing their concentration to 5 μM without laser irradiation. In comparison, obvious necrosis of HeLa cells with 55.2% viability could be detected for the sample treated with as low as 0.3 μM $Au_{44}MBA_{26}$-Cy7 NCs under 808 nm laser irradiation, and <10% HeLa cells survived when treated with ≥2.5 μM of the $Au_{44}MBA_{26}$-Cy7 NCs under the same conditions, while the pristine $Au_{44}MBA_{26}$ NCs began to show PTT activity for cell killing when their concentration was higher than 10 μM (Fig. S11b†). Taken together, both live/dead staining and MTT assays clearly demonstrate that the $Au_{44}MBA_{26}$-Cy7 NCs not only exhibit good biocompatibility, but also show excellent *in vitro* PTT effect. Besides this, we also performed confocal PL microscopy to uncover the uptake behavior of the HeLa cells for the $Au_{44}MBA_{26}$-Cy7 NCs. As shown in Fig. 2g, the HeLa cells show red PL in the cytoplasm after incubation with the $Au_{44}MBA_{26}$-Cy7 NCs. To determine the subcellular distribution, the lysosome-specific staining probe LysoTracker Green and mitochondria-specific staining probe MitoTracker Green were used for co-staining the $Au_{44}MBA_{26}$-Cy7 NCs. The green PL of LysoTracker green is strongly correlated with the red PL channel (Rr = 0.8), indicating that most of the $Au_{44}MBA_{26}$-Cy7 NCs are located within the lysosome (Fig. 2g). Therefore, the above results manifest that the $Au_{44}MBA_{26}$-Cy7 NCs enter the cells through endocytosis.

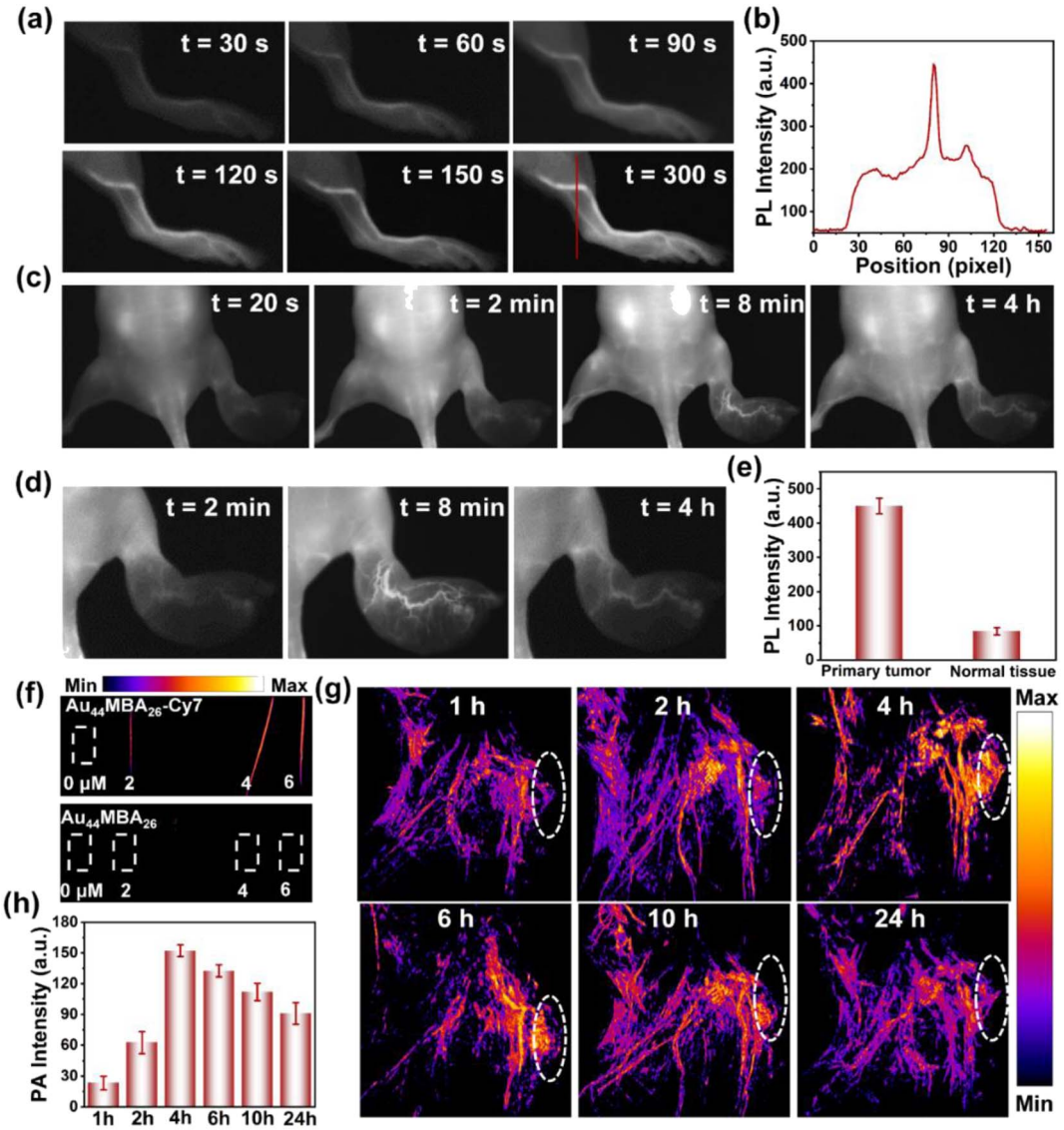

Fig. 3 *In vivo* NIR-II PL and PA imaging. (a) Time-course NIR-II PL images of the hindlimb vessels in mice after the intravenous injection of the $Au_{44}MBA_{26}$-Cy7 NCs. (b) The NIR-II PL line scan profile of the hindlimb vessels in (a). (c) Time-course NIR-II PL images and (d) enlarged images of 4T1 tumor-bearing mice after intravenous injection of the $Au_{44}MBA_{26}$-Cy7 NCs. (e) Comparison of the relative NIR-II PL intensities of the primary tumor and healthy tissue 8 min from NC injection. (f) PA images of pristine $Au_{44}MBA_{26}$ and $Au_{44}MBA_{26}$-Cy7 solutions with concentrations of 0–6 μM. (g) Time-course PA images of 4T1 tumor-bearing mice after intravenous injection of the $Au_{44}MBA_{26}$-Cy7 NCs. The dashed circle indicates the tumor. (h) Time-related relative PA intensities of the $Au_{44}MBA_{26}$-Cy7 NCs in tumor sites based on the quantitative analysis of the circled tumor sites shown in (g).

In addition to the remarkable *in vitro* photothermal properties, the $Au_{44}MBA_{26}$-Cy7 NCs also display prominent performance in noninvasive *in vivo* NIR-II PL and PA imaging. The strong NIR-II PL signal of the $Au_{44}MBA_{26}$-Cy7 NCs allowed high-contrast, real-time NIR-II vessel imaging under 808 nm laser irradiation to be achieved. As shown in Fig. 3a, the hindlimb vessels in mice could be observed with an ultrahigh contrast in the NIR-II window. Specifically, the vessels of the mice were visible at 30 s from the intravenous injection of the $Au_{44}MBA_{26}$-Cy7 NCs, and extremely clear at 120 s. The cross-sectional intensity profile of the mice's hindlimb at 300 s also revealed the intense NIR-II PL signal in the vessels (Fig. 3b). Taken together, one may conclude that the $Au_{44}MBA_{26}$-Cy7 NCs with ultrasmall size exhibit molecule-like pharmacokinetics, possessing great potential in ultradeep NIR-II PL imaging for medical diagnosis.

To test the possibility of NIR-II PL imaging-guided tumor therapy, we further established a metastatic tumor model in which 4T1 cells were inoculated into the right hind paw of nude mice, and checked the usefulness of the $Au_{44}MBA_{26}$-Cy7 NCs for the real-time NIR-II PL imaging of tumors. As shown, after intravenously injecting $Au_{44}MBA_{26}$-Cy7 NCs into the 4T1 tumor-bearing mice, the NIR-II PL signal under 808 nm laser irradiation could be recognized at 20 s (Fig. 3c). Benefiting from the

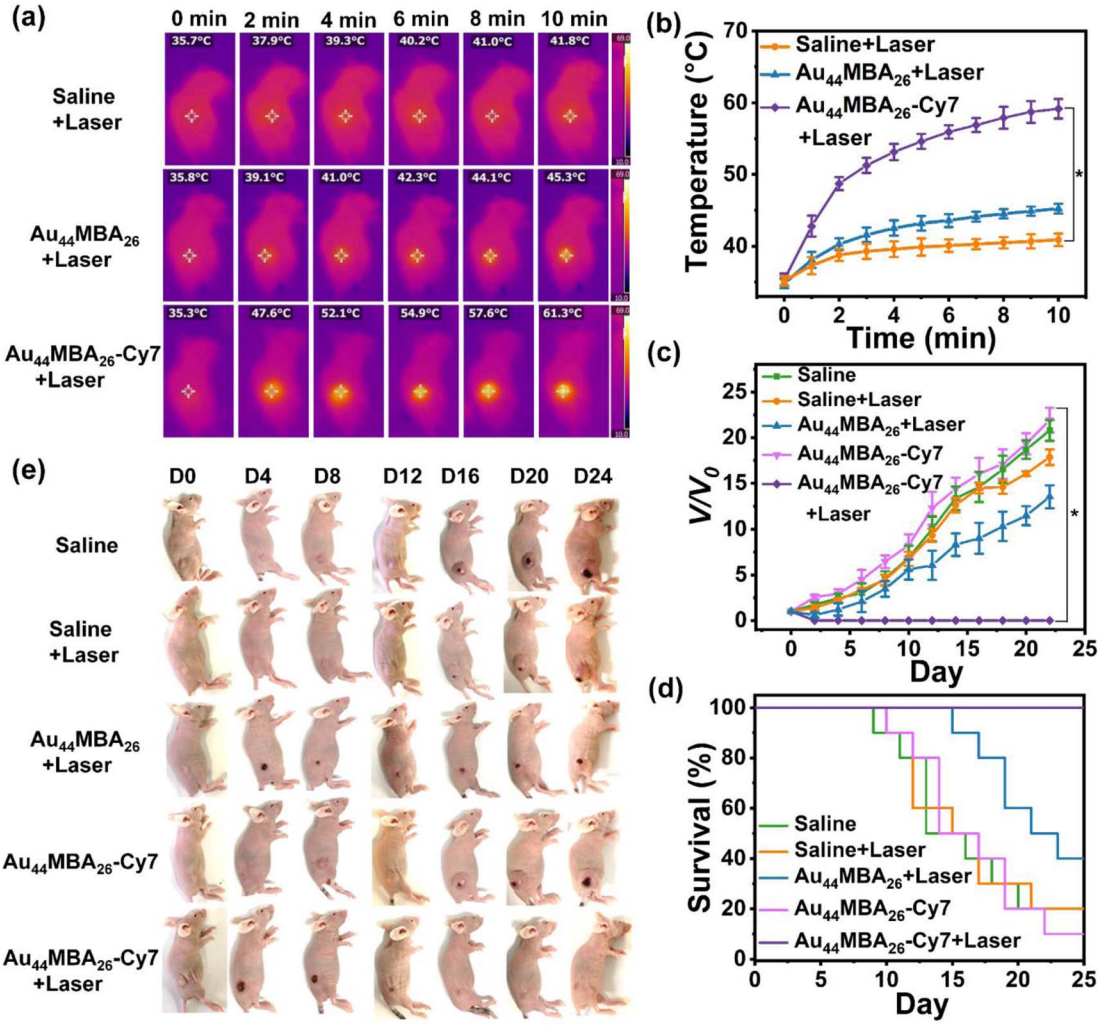

Fig. 4 PTT *in vivo*. (a) Representative IR thermal images of 4T1 tumor-bearing mice injected intravenously with the $Au_{44}MBA_{26}$-Cy7 NCs, $Au_{44}MBA_{26}$ NCs, or saline with 10 min of laser irradiation (808 nm, 1.0 W cm^{-2}). (b) Irradiation time-related temperature elevation curves of the tumor sites. Error bars indicate the mean ± SD ($n = 5$), *$P < 0.05$. (c) The tumor growth curves of 4T1 tumor-bearing mice in different treatment groups. Error bars indicate the mean ± SD ($n = 5$), *$P < 0.05$. (d) The survival plot of the 4T1 tumor-bearing mice in the different treatment groups. (e) Photographs of 4T1 tumor-bearing mice 0, 4, 8, 12, 16, 20, and 24 days after treatment with saline, $Au_{44}MBA_{26}$ NCs, and $Au_{44}MBA_{26}$-Cy7 NCs in the dark or under laser irradiation.

continuous accumulation of the $Au_{44}MBA_{26}$-Cy7 NCs at the tumor site *via* the EPR effect, the NIR-II PL intensity in the primary tumor tissues gradually increased within 8 min, and was five times greater than that in the healthy tissue (Fig. 3c and d), indicating that the $Au_{44}MBA_{26}$-Cy7 NCs have tumor targeting ability and possess significant advantages in NIR-II PL imaging for tumor diagnosis with deep-tissue penetration (Fig. 3e). Furthermore, the NIR-II PL signal of the $Au_{44}MBA_{26}$-Cy7 NCs in primary tumor tissues remained after 4 h with a high resolution (Fig. 3c and d), which suggests their long-lasting imaging ability, supporting their application in long-period NIR-II PL imaging-guided tumor therapy.

One salient feature of the $Au_{44}MBA_{26}$-Cy7 NCs is their dual-mode noninvasive imaging of deep tissues with mutual signal correction. Aside from NIR-II PL imaging, the $Au_{44}MBA_{26}$-Cy7 NCs could simultaneously achieve *in vivo* PA imaging. It should be mentioned that the generation of the PA signal is related to thermal expansion. While an $Au_{44}MBA_{26}$-Cy7 NC solution with a low concentration of 2 μM showed strong PA signals (Fig. 3f), the same was not realized by the pristine $Au_{44}MBA_{26}$ NC solution, although it generated a PA signal when the concentration was increased by ≥10 times (Fig. S12†). This preliminary result implies the capability of the $Au_{44}MBA_{26}$-Cy7 NCs of real-time PA imaging. To further check the applicability for *in vivo* PA imaging, the $Au_{44}MBA_{26}$-Cy7 NCs were injected into 4T1 tumor-bearing mice *via* the tail vein. Owing to the EPR effect, the $Au_{44}MBA_{26}$-Cy7 NCs accumulated continuously at the tumor site, enabling the successful PA imaging of the tumor with a rapidly increasing signal intensity until a maximum was reached at 4 h (Fig. 3g and h), which demonstrated the excellent *in vivo* PA imaging ability of the $Au_{44}MBA_{26}$-Cy7 NCs. Based on the quantitative analysis of the time-related relative PA

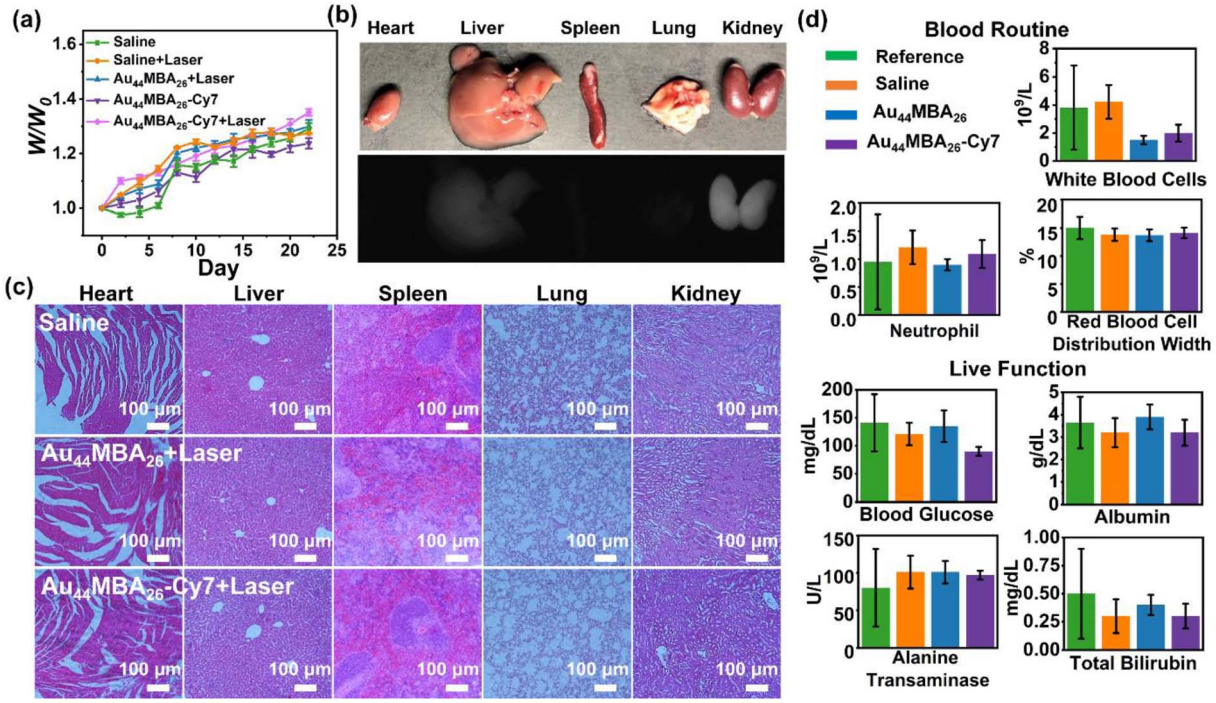

Fig. 5 (a) Body weight changes of the mice in different treatment groups. (b) The bio-distribution of $Au_{44}MBA_{26}$-Cy7 NCs in the heart, liver, spleen, lung, and kidney 24 h after the intravenous injection of the $Au_{44}MBA_{26}$-Cy7 NCs. (c) H & E-stained histological sections of heart, liver, spleen, lung, and kidney tissues obtained from mice in the saline, and PTT groups with the $Au_{44}MBA_{26}$ and $Au_{44}MBA_{26}$-Cy7 NCs. (d) Blood test and liver function parameters for mice intravenously injected with saline, $Au_{44}MBA_{26}$ NCs, or $Au_{44}MBA_{26}$-Cy7 NCs.

intensities of the $Au_{44}MBA_{26}$-Cy7 NCs at the tumor sites (Fig. 3h), we can deduce that 4 h from NCs injection is the optimal time point for *in vivo* PTT. More importantly, the $Au_{44}MBA_{26}$-Cy7 NCs could simultaneously implement NIR-II PL and PA imaging for tumors with both deep-tissue penetration and high spatial resolution at 4 h from NC injection, which may guide cancer PTT in terms of providing precise tumor location and real-time feedback. It is worth noting that the PL and PA attributes with a competitive relationship were successfully integrated into one material in this study, highlighting the strong designability of the $Au_{44}MBA_{26}$-Cy7 NCs *via* ligand engineering.

With the guidance of *in vivo* NIR-II PL and PA imaging, we further investigated the *in vivo* PTT of the $Au_{44}MBA_{26}$-Cy7 NCs for 4T1 tumor-bearing mice. As shown in Fig. 4a and b, the infrared radiation (IR) thermal mapping images of 4T1 tumor-bearing mice treated with the $Au_{44}MBA_{26}$-Cy7 NCs show that the tumor temperature increases rapidly, and reaches the highest temperature of 61.3 °C with 808 nm laser irradiation for 10 min. This result is better than the treatment of the $Au_{44}MBA_{26}$ NCs and saline with temperature elevations of 9.5 °C and 6 °C, respectively. Consequently, the tumors in mice treated with the $Au_{44}MBA_{26}$-Cy7 NCs were successfully ablated upon laser irradiation, and burn scars were generated at the tumor site.

After 16 days, 4T1 tumor-bearing mice treated with the $Au_{44}MBA_{26}$-Cy7 NCs were all healed without tumor recurrence (Fig. 4c and e). In addition, all mice in this group were alive and had to be euthanized (Fig. 4d). By contrast, the tumor of mice treated with the $Au_{44}MBA_{26}$ NCs initially showed a slight decrease, but then began to grow rapidly from the 4th day (Fig. 4c and e). A worse situation was observed in the control groups (*i.e.*, tumor-bearing mice treated with only laser irradiation or $Au_{44}MBA_{26}$-Cy7 NCs) where tumors continued to grow rapidly (Fig. 4c and e). In comparison to the recovered health status of mice treated with PTT using the $Au_{44}MBA_{26}$-Cy7 NCs, the average life span of mice in the other four groups was only 17–21 days (Fig. 4d). Such excellent PTT efficacy of the $Au_{44}MBA_{26}$-Cy7 NCs is expected considering their outstanding photothermal efficiency, decent molecular pharmacokinetics, good tumor selectivity (due to the EPR effect), and benign biocompatibility. On this basis, we can conclude that the $Au_{44}MBA_{26}$-Cy7 NCs have been demonstrated to be efficient in NIR-II PL and PA imaging-guided cancer PTT, realizing the first successful attempt in designing an Au NC-based molecular theranostic probe for noninvasive NIR-II PL and PA imaging-guided cancer PTT.

In addition, the possible adverse effects of the $Au_{44}MBA_{26}$-Cy7 NCs on mice were also examined. Firstly, we checked the body weights of mice in each group during the whole PTT process. The results show that no remarkable weight variation was observed between the different groups of the mice (Fig. 5a), indicating that $Au_{44}MBA_{26}$-Cy7 NCs-directed PTT had almost no adverse effects on the mice. In addition, after 24 h from the intravenous injection of the $Au_{44}MBA_{26}$-Cy7 NCs, the mice were sacrificed and dissected in order to evaluate the influence of the

$Au_{44}MBA_{26}$-Cy7 NCs on their major organs (*i.e.*, heart, liver, spleen, lung and kidney). As shown in Fig. 5b, no NIR-II PL signal was perceived from the heart, spleen, and lung, while a moderate PL signal emanated from the kidney and a weak PL signal from the liver was detected. These results suggest the good renal clearance of the ultrasmall $Au_{44}MBA_{26}$-Cy7 NCs, further reflecting their good biosafety in *in vivo* dual-mode imaging-guided PTT. Moreover, the haematoxylin and eosin (H & E) histopathological assessment of the major organs of mice in each group disclosed that there is no significant difference in the organs after PTT (Fig. 5c), which indicates that the dual-mode imaging-guided PTT with the $Au_{44}MBA_{26}$-Cy7 NCs did not damage the major organs of the mice. Besides this, the blood and liver function of the tumor-bearing mice treated with saline, $Au_{44}MBA_{26}$ NCs, and $Au_{44}MBA_{26}$-Cy7 NCs were further evaluated. Routine blood tests revealed that the white blood cell, neutrophil and red blood cell counts were all unaffected by the PTT, corroborating the safety and low toxicity of the $Au_{44}MBA_{26}$-Cy7 NCs and PTT (Fig. 5d). Liver function tests show no significant differences between the three mice groups, and all parameters, including blood glucose, albumin, alanine, and total bilirubin, were within the reference range, indicating that the treated mice exhibited basically normal liver function (Fig. 5d). All of these results exemplify the perfect biosafety of PTT using the $Au_{44}MBA_{26}$-Cy7 NCs.

Conclusions

In this study, we developed a novel Au NC-based theranostics probe for ultradeep NIR-II PL and PA imaging-guided cancer PTT. The key to this design is the ligand engineering of NIR-II emitting $Au_{44}MBA_{26}$ NCs by rigid PA/photothermal Cy7 molecules *via* click chemistry. This not only enhanced the NIR-II PL intensity of the Au_{44} NCs *via* AIE, but also elevated their photothermal efficiency to 65.12% by offering a highly localized Cy7 concentration on the NC surface, contradicting the Jablonski energy spectrum theory that strong PL signal and excellent photothermal properties cannot be attained simultaneously. Owing to the EPR effect, the as-synthesized $Au_{44}MBA_{26}$ NCs-Cy7 NCs successfully achieved *in vivo* NIR-II PL and PA imaging of tumors in real time with deep tissue penetration, high sensitivity and specificity, which enabled them to be capable of guiding cancer PTT by offering accurate tumor location and real-time feedback. In particular, the 4T1 tumor-bearing mice could be healed without tumor recurrence upon PTT using the $Au_{44}MBA_{26}$-Cy7 NCs by efficiently ablating tumors. In addition, comprehensive studies revealed that the $Au_{44}MBA_{26}$-Cy7 NCs exhibit neglectable cytotoxicity and good biosafety in terms of good renal clearance, no damage to major organs, and unaffected blood and liver functions, confirming the feasible application of the $Au_{44}MBA_{26}$-Cy7 NCs for noninvasive NIR-II PL and PA imaging-guided cancer PTT. This study is interesting because it provides a paradigm in the design of metal NCs-based multifunctional biomedicine for disease theranostics. We envision that the $Au_{44}MBA_{26}$-Cy7 NCs may have great potential for future clinical translation, which may stimulate additional research activities in noninvasive imaging-guided disease therapy.

Data availability

All experimental supporting data and procedures are available in the ESI.†

Author contributions

J. P. X., X. F. Z., and X. Y. conceived and supervised the project. G. Y. performed the experiments, and collected and analyzed the data. X. L. M., X. X. P., Y. T., Q. F. Y., Y. R. W., F. Y. J., and F. L. D. helped with the data collection and analysis of animal experiments. G. Y. and X. Y. co-wrote the manuscript. All authors discussed the results and commented on the manuscript. All authors approved the final version of the manuscript.

Conflicts of interest

There are no conflicts to declare.

Acknowledgements

This work was supported by the National Natural Science Foundation of China (22071127, 22071174), the Taishan Scholar Foundation (tsqn201812074), the Natural Science Foundation of Shandong Province (ZR2019YQ07), and the Academic Research Grants from the Ministry of Education of Singapore (R-279-000-580-112 and R-279-000-538-114). This study was performed in strict accordance with the NIH guidelines for the care and use of laboratory animals (NIH Publication No. 85–23 Rev. 1985) and was approved by the Biomedical Ethics Committee of Qingdao Zhong Hao Biological Engineering Co., Ltd. (Qingdao, China).

References

1 (*a*) B. Chen, Y. Yan, Y. Yang, G. Cao, X. Wang, Y. Wang, F. Wan, Q. Yin, Z. Wang, Y. Li, L. Wang, B. Xu, F. You, Q. Zhang and Y. Wang, *Nat. Nanotechnol.*, 2022, **17**(7), 788–798; (*b*) J. Zhang, L. Ning, J. Huang, C. Zhang and K. Pu, *Chem. Sci.*, 2020, **11**, 618–630; (*c*) N. Niu, Y. Yu, Z. Zhang, M. Kang, L. Wang, Z. Zhao, D. Wang and B. Z. Tang, *Chem. Sci.*, 2022, **13**, 5929–5937; (*d*) H.-T. Feng, S. Zou, M. Chen, F. Xiong, M.-H. Lee, L. Fang and B. Z. Tang, *J. Am. Chem. Soc.*, 2020, **142**, 11442; (*e*) J. K. Tee, L. X. Yip, E. S. Tan, S. Santitewagun, A. Prasath, P. C. Ke, H. K. Ho and D. T. Leong, *Chem. Soc. Rev.*, 2019, **48**, 5381; (*f*) D. Y. Oh, S. S. Kwek, S. S. Raju, T. Li, E. McCarthy, E. Chow, D. Aran, A. Ilano, C.-C. S. Pai, C. Rancan, K. Allaire, A. Burra, Y. Sun, M. H. Spitzer, S. Mangul, S. Porten, M. V. Meng, T. W. Friedlander, C. J. Ye and L. Fong, *Cell*, 2020, **181**, 1612.

2 (*a*) L. V. Wang and S. Hu, *Science*, 2012, **335**, 1458; (*b*) A. L. Antaris, H. Chen, K. Cheng, Y. Sun, G. Hong, C. Qu, S. Diao, Z. Deng, X. Hu, B. Zhang, X. Zhang, O. K. Yaghi, Z. R. Alamparambil, X. Hong, Z. Cheng and H. Dai, *Nat. Mater.*, 2016, **15**, 235; (*c*) Y. Liu, P. Bhattarai, Z. Dai and X. Chen, *Chem. Soc. Rev.*, 2019, **48**, 2053; (*d*) X. Li, T. Yong,

Z. Wei, N. Bie, X. Zhang, G. Zhan, J. Li, J. Qin, J. Yu, B. Zhang, L. Gan and X. Yang, *Nat. Commun.*, 2022, **13**, 2794.

3 J. Qi, C. Chen, X. Zhang, X. Hu, S. Ji, R. T. K. Kwok, J. W. Y. Lam, D. Ding and B. Z. Tang, *Nat. Commun.*, 2018, **9**, 1848.

4 (*a*) B. Du, X. Jiang, A. Das, Q. Zhou, M. Yu, R. Jin and J. Zheng, *Nat. Nanotechnol.*, 2017, **12**, 1096; (*b*) J. Huang, X. Chen, Y. Jiang, C. Zhang, S. He, H. Wang and K. Pu, *Nat. Mater.*, 2022, **21**, 598.

5 (*a*) P. N. Duchesne, Z. Y. Li, C. P. Deming, V. Fung, X. Zhao, J. Yuan, T. Regier, A. Aldalbahi, Z. Almarhoon, S. Chen, D.-e. Jiang, N. Zheng and P. Zhang, *Nat. Mater.*, 2018, **17**, 1033; (*b*) M. Han, M. Guo, Y. Yun, Y. Xu, H. Sheng, Y. Chen, Y. Du, K. Ni, Y. Zhu and M. Zhu, *Adv. Funct. Mater.*, 2022, **32**, 2202820; (*c*) X. Kang, Y. Li, M. Zhu and R. Jin, *Chem. Soc. Rev.*, 2020, **49**, 6443; (*d*) I. Chakraborty and T. Pradeep, *Chem. Rev.*, 2017, **117**, 8208; (*e*) C. Yao, N. Guo, S. Xi, C.-Q. Xu, W. Liu, X. Zhao, J. Li, H. Fang, J. Su, Z. Chen, H. Yan, Z. Qiu, P. Lyu, C. Chen, H. Xu, X. Peng, X. Li, B. Liu, C. Su, S. J. Pennycook, C.-J. Sun, J. Li, C. Zhang, Y. Du and J. Lu, *Nat. Commun.*, 2020, **11**, 4389.

6 (*a*) M. R. Narouz, K. M. Osten, P. J. Unsworth, R. W. Y. Man, K. Salorinne, S. Takano, R. Tomihara, S. Kaappa, S. Malola, C.-T. Dinh, J. D. Padmos, K. Ayoo, P. J. Garrett, M. Nambo, J. H. Horton, E. H. Sargent, H. Häkkinen, T. Tsukuda and C. M. Crudden, *Nat. Chem.*, 2019, **11**, 419; (*b*) X. Yuan, B. Zhang, Z. Luo, Q. Yao, D. T. Leong, N. Yan and J. Xie, *Angew. Chem., Int. Ed.*, 2014, **53**, 4623; (*c*) T. Kawawaki, Y. Kataoka, M. Hirata, Y. Akinaga, R. Takahata, K. Wakamatsu, Y. Fujiki, M. Kataoka, S. Kikkawa, A. S. Alotabi, S. Hossain, D. J. Osborn, T. Teranishi, G. G. Andersson, G. F. Metha, S. Yamazoe and Y. Negishi, *Angew. Chem., Int. Ed.*, 2021, **60**, 21340; (*d*) H. Shen, Q. Wu, S. Malola, Y.-Z. Han, Z. Xu, R. Qin, X. Tang, Y.-B. Chen, B. K. Teo, H. Häkkinen and N. Zheng, *J. Am. Chem. Soc.*, 2022, **144**, 10844.

7 (*a*) M. Zhou, T. Higaki, G. Hu, Y. Sfeir Matthew, Y. Chen, D.-e. Jiang and R. Jin, *Science*, 2019, **364**, 279; (*b*) M. R. Narouz, S. Takano, P. A. Lummis, T. I. Levchenko, A. Nazemi, S. Kaappa, S. Malola, G. Yousefalizadeh, L. A. Calhoun, K. G. Stamplecoskie, H. Häkkinen, T. Tsukuda and C. M. Crudden, *J. Am. Chem. Soc.*, 2019, **141**, 14997; (*c*) C. Zhu, J. Xin, J. Li, H. Li, X. Kang, Y. Pei and M. Zhu, *Angew. Chem., Int. Ed.*, 2022, e202205947; (*d*) J.-J. Li, C.-Y. Liu, Z.-J. Guan, Z. Lei and Q.-M. Wang, *Angew. Chem., Int. Ed.*, 2022, **61**, e202201549.

8 (*a*) X.-Q. Liang, Y.-Z. Li, Z. Wang, S.-S. Zhang, Y.-C. Liu, Z.-Z. Cao, L. Feng, Z.-Y. Gao, Q.-W. Xue, C.-H. Tung and D. Sun, *Nat. Commun.*, 2021, **12**, 4966; (*b*) J.-Q. Wang, Z.-J. Guan, W.-D. Liu, Y. Yang and Q.-M. Wang, *J. Am. Chem. Soc.*, 2019, **141**, 2384; (*c*) K. R. Krishnadas, L. Sementa, M. Medves, A. Fortunelli, M. Stener, A. Fürstenberg, G. Longhi and T. Bürgi, *ACS Nano*, 2020, **14**, 9687.

9 (*a*) Y. Li, M. Zhou, Y. Song, T. Higaki, H. Wang and R. Jin, *Nature*, 2021, **594**, 380; (*b*) X. Cai, W. Hu, S. Xu, D. Yang, M. Chen, M. Shu, R. Si, W. Ding and Y. Zhu, *J. Am. Chem. Soc.*, 2020, **142**, 4141; (*c*) H. Seong, V. Efremov, G. Park, H. Kim, J. S. Yoo and D. Lee, *Angew. Chem., Int. Ed.*, 2021, **60**, 14563; (*d*) X. Yuan, L. L. Chng, J. Yang and J. Y. Ying, *Adv. Mater.*, 2020, **32**, 1906063; (*e*) L.-J. Liu, Z.-Y. Wang, Z.-Y. Wang, R. Wang, S.-Q. Zang and T. C. W. Mak, *Angew. Chem., Int. Ed.*, 2022, e202205626; (*f*) X. Wang, L. Zhao, X. Li, Y. Liu, Y. Wang, Q. Yao, J. Xie, Q. Xue, Z. Yan, X. Yuan and W. Xing, *Nat. Commun.*, 2022, **13**, 1596.

10 (*a*) M. Yu, J. Xu and J. Zheng, *Angew. Chem., Int. Ed.*, 2019, **58**, 4112; (*b*) K. Zheng and J. Xie, *Trends Chem.*, 2020, **2**, 665.

11 (*a*) X. Jiang, B. Du and J. Zheng, *Nat. Nanotechnol.*, 2019, **14**, 874; (*b*) J. Liu, M. Yu, X. Ning, C. Zhou, S. Yang and J. Zheng, *Angew. Chem., Int. Ed.*, 2013, **52**, 12572; (*c*) C.-Y. Liu, S.-F. Yuan, S. Wang, Z.-J. Guan, D.-e. Jiang and Q.-M. Wang, *Nat. Commun.*, 2022, **13**, 2082.

12 (*a*) C. N. Loynachan, A. P. Soleimany, J. S. Dudani, Y. Lin, A. Najer, A. Bekdemir, Q. Chen, S. N. Bhatia and M. M. Stevens, *Nat. Nanotechnol.*, 2019, **14**, 883; (*b*) B. Du, M. Yu and J. Zheng, *Nat. Rev. Mater.*, 2018, **3**, 358.

13 (*a*) X. Zhang, Z. Zhang, Q. Shu, C. Xu, Q. Zheng, Z. Guo, C. Wang, Z. Hao, X. Liu, G. Wang, W. Yan, H. Chen and C. Lu, *Adv. Funct. Mater.*, 2021, **31**, 2008720; (*b*) K. Zheng, K. Li, T.-H. Chang, J. Xie and P.-Y. Chen, *Adv. Funct. Mater.*, 2019, **29**, 1904603; (*c*) Y. Hua, J.-H. Huang, Z.-H. Shao, X.-M. Luo, Z.-Y. Wang, J.-Q. Liu, X. Zhao, X. Chen and S.-Q. Zang, *Adv. Mater.*, 2022, 2203734; (*d*) O.-V. Pham-Nguyen, J. Shin, Y. Park, S. Jin, S. R. Kim, Y. M. Jung and H. S. Yoo, *Biomacromolecules*, 2022, **23**, 3130; (*e*) S. M. van de Looij, E. R. Hebels, M. Viola, M. Hembury, S. Oliveira and T. Vermonden, *Bioconjugate Chem.*, 2022, **33**, 4.

14 (*a*) H. Liu, G. Hong, Z. Luo, J. Chen, J. Chang, M. Gong, H. He, J. Yang, X. Yuan, L. Li, X. Mu, J. Wang, W. Mi, J. Luo, J. Xie and X.-D. Zhang, *Adv. Mater.*, 2019, **31**, 1901015; (*b*) X. Song, W. Zhu, X. Ge, R. Li, S. Li, X. Chen, J. Song, J. Xie, X. Chen and H. Yang, *Angew. Chem., Int. Ed.*, 2021, **60**, 1306; (*c*) W. Wang, Y. Kong, J. Jiang, Q. Xie, Y. Huang, G. Li, D. Wu, H. Zheng, M. Gao, S. Xu, Y. Pan, W. Li, R. Ma, M. X. Wu, X. Li, H. Zuilhof, X. Cai and R. Li, *Angew. Chem., Int. Ed.*, 2020, **59**, 22431; (*d*) D. Li, Q. Liu, Q. Qi, H. Shi, E.-C. Hsu, W. Chen, W. Yuan, Y. Wu, S. Lin, Y. Zeng, Z. Xiao, L. Xu, Y. Zhang, T. Stoyanova, W. Jia and Z. Cheng, *Small*, 2020, **16**, 2003851; (*e*) Y. Chen, D. M. Montana, H. Wei, J. M. Cordero, M. Schneider, X. Le Guével, O. Chen, O. T. Bruns and M. G. Bawendi, *Nano Lett.*, 2017, **17**, 6330.

15 (*a*) X. Mu, Y. Lu, F. Wu, Y. Wei, H. Ma, Y. Zhao, J. Sun, S. Liu, X. Zhou and Z. Li, *Adv. Mater.*, 2020, **32**, 1906711; (*b*) J. Chen, M. Gong, Y. Fan, J. Feng, L. Han, H. L. Xin, M. Cao, Q. Zhang, D. Zhang, D. Lei and Y. Yin, *ACS Nano*, 2022, **16**, 910; (*c*) G. Xu, C. Li, C. Chi, L. Wu, Y. Sun, J. Zhao, X.-H. Xia and S. Gou, *Nat. Commun.*, 2022, **13**, 3064.

16 (*a*) X. Jiang, B. Du, S. Tang, J.-T. Hsieh and J. Zheng, *Angew. Chem., Int. Ed.*, 2019, **58**, 5994; (*b*) M. Y. Lucero and J. Chan, *Nat. Chem.*, 2021, **13**, 1248; (*c*) C. A. Wood, S. Han, C. S. Kim, Y. Wen, D. R. T. Sampaio, J. T. Harris, K. A. Homan, J. L. Swain, S. Y. Emelianov, A. K. Sood, J. R. Cook,

K. V. Sokolov and R. R. Bouchard, *Nat. Commun.*, 2021, **12**, 5410.

17 (*a*) M. Zhang, W. Wang, M. Mohammadniaei, T. Zheng, Q. Zhang, J. Ashley, S. Liu, Y. Sun and B. Z. Tang, *Adv. Mater.*, 2021, **33**, 2008802; (*b*) Z. Wu, Q. Yao, O. J. H. Chai, N. Ding, W. Xu, S. Zang and J. Xie, *Angew. Chem., Int. Ed.*, 2020, **59**, 9934; (*c*) D. Yan, M. Wang, Q. Wu, N. Niu, M. Li, R. Song, J. Rao, M. Kang, Z. Zhang, F. Zhou, D. Wang and B. Z. Tang, *Angew. Chem., Int. Ed.*, 2022, e202202614; (*d*) Z. Luo, X. Yuan, Y. Yu, Q. Zhang, D. T. Leong, J. Y. Lee and J. Xie, *J. Am. Chem. Soc.*, 2012, **134**, 16662.

18 X. Zhang, Z. Wang, S. Qian, N. Liu, L. Sui and X. Yuan, *Nanoscale*, 2020, **12**, 6449.

19 Q. Yao, X. Yuan, V. Fung, Y. Yu, D. T. Leong, D.-e. Jiang and J. Xie, *Nat. Commun.*, 2017, **8**, 927.

20 K. Pyo, V. D. Thanthirige, S. Y. Yoon, G. Ramakrishna and D. Lee, *Nanoscale*, 2016, **8**, 20008–20016.

21 H. Deng, K. Huang, L. Xiu, W. Sun, Q. Yao, X. Fang, X. Huang, H. A. A. Noreldeen, H. Peng, J. Xie and W. Chen, *Nat. Commun.*, 2022, **13**, 3381.

22 Y.-S. Chen and P. V. Kamat, *J. Am. Chem. Soc.*, 2014, **136**, 6075.

23 L. Liao, S. Zhuang, C. Yao, N. Yan, J. Chen, C. Wang, N. Xia, X. Liu, M.-B. Li, L. Li, X. Bao and Z. Wu, *J. Am. Chem. Soc.*, 2016, **138**, 10425.

24 (*a*) C. Iserman, C. Desroches Altamirano, C. Jegers, U. Friedrich, T. Zarin, A. W. Fritsch, M. Mittasch, A. Domingues, L. Hersemann, M. Jahnel, D. Richter, U.-P. Guenther, M. W. Hentze, A. M. Moses, A. A. Hyman, G. Kramer, M. Kreysing, T. M. Franzmann and S. Alberti, *Cell*, 2020, **181**, 818; (*b*) C. Spiess, A. Beil and M. Ehrmann, *Cell*, 1999, **97**, 339.

25 X. Cai, X. Jia, W. Gao, K. Zhang, M. Ma, S. Wang, Y. Zheng, J. Shi and H. Chen, *Adv. Funct. Mater.*, 2015, **25**, 2520.